γ-Al₂O₃-Supported and Unsupported (Ni)MoS₂ for the Hydrodenitrogenation of Quinoline in the Presence of Dibenzothiophene

Jennifer Hein, Ana Hrabar, Andreas Jentys, Oliver Y. Gutiérrez,* and Johannes A. Lercher*[a]

Supported $MoS_2/\gamma\text{-}Al_2O_3$ and $Ni\text{-}MoS_2/\gamma\text{-}Al_2O_3$ as well as unsupported $Ni\text{-}MoS_2$ were investigated in the hydrodenitrogenation (HDN) of quinoline in the presence of dibenzothiophene (DBT). The supported oxide catalyst precursors had a well-dispersed amorphous polymolybdate structure that led to the formation of a highly dispersed sulfide phase. In contrast, the unsupported catalyst precursor consisted of a mixture of nickel molybdate and ammonium nickel molybdate phases that formed stacked sulfide slabs after sulfidation. On all catalysts, the reaction pathway for the removal of N in quinoline HDN mainly followed the sequence quinoline→1,2,3,4-tetrahydroquinoline→decahydroquinoline→propylcyclohexylamine→propylcyclohexene→propylcyclohexane. The hydrodesulfurization of DBT proceeded mainly by direct desulfurization towards biphenyl. For both processes, the activity increased in the order $MoS_2/\gamma\text{-}Al_2O_3 < Ni\text{-}MoS_2/\text{unsupported} < Ni\text{-}MoS_2/\gamma\text{-}Al_2O_3$. The promotion of the MoS_2 phase with Ni enhances the activity of the unsupported catalyst to a greater extent than the supported one. However, the multiply stacked unsupported $Ni\text{-}MoS_2$ exhibited lower rates than $Ni\text{-}MoS_2/\gamma\text{-}Al_2O_3$ because of its lower dispersion.

Introduction

Hydrodefunctionalization and hydrogenation catalyzed by sulfide catalysts are key processes to obtain clean fuels. The increasing need to improve the efficiency of refining processes has stimulated a large number of fundamental studies on Ni- and/or Co-promoted MoS_2.[1,2] One of the main challenges in the understanding of these materials is the large number of (structurally and chemically) different adsorption sites, which may all be potentially active for H_2 activation, hydrogenation, and C—S and C—N bond cleavage. Coordinatively unsaturated sites (CUS), that is, exposed metal cations, act as Lewis acid sites for the adsorption of electron-pair donors such as S- and N-containing compounds. The —SH groups at the termination of the sulfide slabs are Brønsted acidic and provide hydrogen for hydrogenolysis and hydrogenation. The existence of metal-like states on the basal planes close to the edge of the basal plane has also been proposed.[3] In addition to the nature of the MoS_2 sites, the type of support and the presence of promoters influence the properties of the catalyst. Both promoter and support may affect the dispersion and structure of the MoS_2 phase as well as its intrinsic activity.

It has been demonstrated that the morphology of the MoS_2 plays a major role in the activity and selectivity of the catalyst.

For instance, the rim–edge model rationalizes that the hydrodesulfurization (HDS) functionality of the MoS_2 slabs depends on shape and size of the MoS_2 particles.[4] Although for the HDS of dibenzothiophenes several structure–activity correlations have been proposed,[5–7] only a few attempts to determine the influence of the support, promoter, and morphology of MoS_2 on the functionality of active sites in hydrodenitrogenation (HDN) have been reported.[8–11]

This study aims, therefore, to gain an insight into the role of the promoter and the support on the activity of MoS_2 and to identify the active sites in HDN. Both goals are essential to gain a deeper understanding of the morphology–functionality relationship to design improved HDN catalysts rationally. The physicochemical properties and molecular structures of a series of supported $MoS_2/\gamma\text{-}Al_2O_3$ and $Ni\text{-}MoS_2/\gamma\text{-}Al_2O_3$ catalysts as well as an unsupported $Ni\text{-}MoS_2$ catalyst are described in detail. The performance of the catalysts is explored with respect to the HDN of quinoline (Q) in the presence of dibenzothiophene (DBT). The impact of the support and Ni promoter as well as the functionality of the active sites is discussed by using the detailed physicochemical and kinetic characterization of the sulfide catalysts.

[a] Dipl.-Chem. J. Hein, Dr. A. Hrabar, Dr. A. Jentys, Dr. O. Y. Gutiérrez, Prof. Dr. J. A. Lercher
Lehrstuhl für Technische Chemie 2
Technische Universität München
Lichtenbergstraße 4, D-85747 Garching (Germany)
Fax: (+49) 89 28913544
E-mail: oliver.gutierrez@mytum.de
       johannes.lercher@ch.tum.de

Results

Characterization of oxide precursors and in situ sulfidation studies

The supported oxide precursors are referred as $Mo/\gamma\text{-}Al_2O_3$ and $NiMo/\gamma\text{-}Al_2O_3$, whereas the precursor of the unsupported catalyst is denoted as NiMo/unsupported. The physicochemical properties of the oxide catalyst precursors are compiled in

Table 1. The Mo concentration was 8.6 wt% in both supported catalysts, which corresponds to 2.5 Mo atoms nm^{-2}. The Ni concentration in the NiMo supported catalyst was 3.6 wt% Ni, that is, a molar fraction of 0.4 for Ni. In the unsupported material, the Mo and Ni concentrations were 38 and 25 wt%, respectively, that is, a Ni molar fraction of 0.5.

Table 1. Physicochemical properties of the Mo/γ-Al$_2$O$_3$, NiMo/γ-Al$_2$O$_3$, and NiMo/unsupported oxide catalyst precursors.

Catalyst	Metal conc. [wt%] Mo	Ni	Ni molar fraction	Surface area [m^{2}g^{-1}]	Pore volume [cm^{3}g^{-1}]	Pore diameter [nm]
γ-Al$_2$O$_3$	–	–	–	237	0.75	8.8
Mo/γ-Al$_2$O$_3$	8.6	–	–	220	0.62	8.5
NiMo/γ-Al$_2$O$_3$	8.6	3.6	0.4	206	0.60	8.5
NiMo/unsupported	38.2	25.1	0.5	26	–	–

We acknowledge that the properties of the oxide precursors and their sulfidation processes may be decisive for the properties of the corresponding sulfide catalysts. However, for the sake of brevity, we present the results of the characterization of the oxide precursors as well as the results of the in situ sulfidation studies in the Supporting Information. In the following, we focus on the physicochemical and kinetic properties of the sulfide catalysts.

Sulfide catalysts

The supported sulfide catalysts are denoted as MoS$_2$/γ-Al$_2$O$_3$ and Ni-MoS$_2$/γ-Al$_2$O$_3$. The unsupported sulfide catalyst is denoted as Ni-MoS$_2$/unsupported. The total NO uptake during adsorption at room temperature was 130, 160, and 66 µmol g$_{cat}^{-1}$ for MoS$_2$/γ-Al$_2$O$_3$, Ni-MoS$_2$/γ-Al$_2$O$_3$, and Ni-MoS$_2$/unsupported, respectively. Recently, it has been shown that NO may adsorb as mononitrosyl or dinitrosyl species on metal cations.[12] To quantitatively discuss the results, it is assumed that NO adsorbs as dinitrosyl species.[13] The concentration of the adsorption sites is thus 65 µmol*g$_{cat}^{-1}$ for MoS$_2$/γ-Al$_2$O$_3$, 80 µmol*g$_{cat}^{-1}$ for Ni-MoS$_2$/γ-Al$_2$O$_3$, and 33 µmol*g$_{cat}^{-1}$ for Ni-MoS$_2$/unsupported. The lower concentration of accessible sites on Ni-MoS$_2$/unsupported is attributed to a highly agglomerated sulfide phase. For the supported catalysts, the increase in the concentration of coordinatively unsaturated sites (23%) after Ni addition was far lower than the concentration of Ni added (68%). We conclude that NO does not adsorb selectively on Ni and that Ni cations are randomly distributed on the MoS$_2$ phase.

The XRD patterns of the sulfided catalysts and reference sulfide materials are given in Figure 1. Supported MoS$_2$/γ-Al$_2$O$_3$ and Ni-MoS$_2$/γ-Al$_2$O$_3$ exhibit two diffraction signals at around 2θ = 33 and 58° attributed to the (100) plane with an interplanar distance of 2.7 Å and to the (110) plane with an interplanar distance of 1.6 Å of MoS$_2$, respectively. The signal at 2θ = 14°, characteristic of the (002) plane with an interplanar distance of 6.1 Å,[14] was not observed, probably because of the
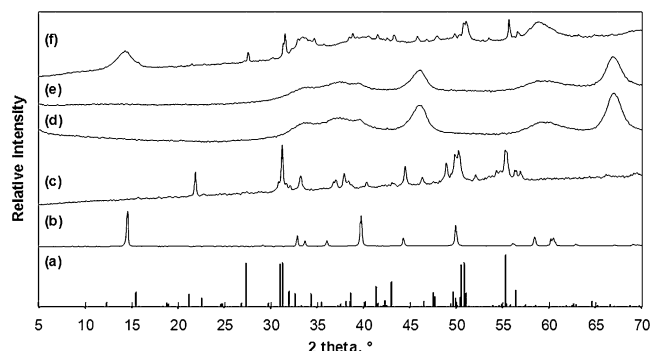

Figure 1. Stick pattern of a) Ni$_9$S$_8$ (ICSD # 63080) and XRD patterns of: b) MoS$_2$, c) Ni$_3$S$_2$, d) MoS$_2$/γ-Al$_2$O$_3$, e) Ni-MoS$_2$/γ-Al$_2$O$_3$, and f) Ni-MoS$_2$/unsupported.

low degree of stacking in the MoS$_2$ particles. The XRD pattern of the Ni-MoS$_2$/unsupported catalyst exhibited well-defined reflections at 2θ = 14, 33, 40, 50, and 59°, which correspond to MoS$_2$, and 2θ = 27, 31, 33, 51, and 56°, which correspond to Ni$_9$S$_8$ (traces of the Ni$_3$S$_2$ and Ni$_3$S$_4$ phases were also identified). The relatively high intensity of the reflection at 2θ = 14° indicates a significantly higher degree of stacking in Ni-MoS$_2$/unsupported than in MoS$_2$/γ-Al$_2$O$_3$ and Ni-MoS$_2$/γ-Al$_2$O$_3$. The full width at half maximum (FWHM) at 2θ = 14° was 2.1°, which is related to an average crystal size of around 40 Å (using the Scherrer equation), corresponds to a stacking degree (number of MoS$_2$ slabs in an average MoS$_2$ particle) of 7.

Selected TEM micrographs of the supported sulfided catalysts are shown in Ref. [15]. The distribution of the number of layers that form the MoS$_2$ clusters and their length calculated from the micrographs are shown in Figure 2.

Typical fringes that correspond to the MoS$_2$ phase were observed with an average length of 7.2 and 5.4 nm for MoS$_2$/γ-Al$_2$O$_3$ and Ni-MoS$_2$/γ-Al$_2$O$_3$, respectively. The average stacking
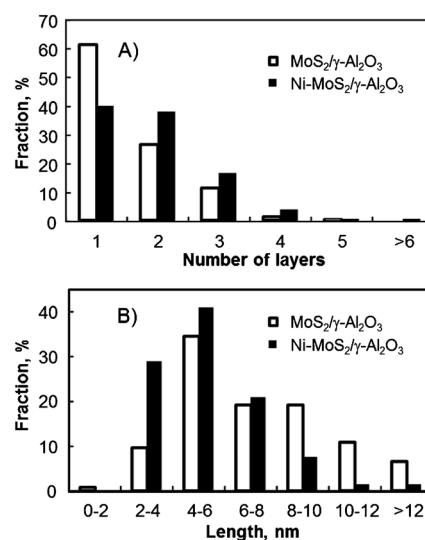
Figure 2. A) Number of layers and B) length of the MoS$_2$ particles in MoS$_2$/γ-Al$_2$O$_3$ and Ni-MoS$_2$/γ-Al$_2$O$_3$ calculated from representative TEM micrographs (shown in Ref. [15]).

degree was 1.6 for $MoS_2/\gamma-Al_2O_3$ and 1.9 for $Ni-MoS_2/\gamma-Al_2O_3$. The stacking degree of only very few MoS_2 particles exceeded three sulfide layers, which confirms a good dispersion of the sulfided slabs on $\gamma-Al_2O_3$ as suggested by the absence of the reflection at $2\theta = 14°$ in the XRD pattern.

The TEM micrographs of the unsupported sulfide catalyst showed the existence of highly stacked and bent MoS_2 particles (Figure 3 A). The characteristic curvature is a consequence of rapid growth along the basal plane and very slow growth along the c axis.[16] The interplanar distance between the two Mo layers in the (0 0 2) direction was approximately 6 Å, with an average stacking degree between 4 and 7. However, it is difficult to define the limits of the MoS_2 clusters in the unsupported catalyst. Therefore, we did not attempt to determine the length and stacking distributions. Diffraction patterns of selected areas were obtained for the unsupported sulfide catalyst; a representative example is shown in Figure 3 B. The continuous rings observed in the electron diffraction patterns result from MoS_2, present as small particles. Additionally, highly crystalline phases were found (single dots in the pattern) and identified as Ni_9S_8 and Ni_3S_4. These findings are in good agreement with the XRD characterization. The high-resolution (HR) SEM micrographs coupled with energy-dispersive X-ray spectroscopy (EDX) clearly showed that large Ni_xS_y crystals are present, which are partially covered by the MoS_2 structures. This means that the MoS_2 particles engulf the nickel sulfide crystals and they are, therefore, difficult to observe in TEM micrographs.

Representative Raman spectra of $MoS_2/\gamma-Al_2O_3$, $Ni-MoS_2/\gamma-Al_2O_3$, and $Ni-MoS_2/unsupported$ catalysts are compiled in Figure 4. Bands related to the MoS_2 phase (Figure 4 b) were found in all three samples, that is, 287, 383, and 409 cm^{-1} that correspond to the S—Mo—S vibration along the basal plane, the Mo—S vibration along the basal plane, and the S—Mo—S vibration along the c axis, respectively.[17,18] The presence of Ni sulfides in the Ni-containing catalysts could not be confirmed by this technique probably because of their low Raman activity (the reference Ni_3S_2 material did not exhibit any band).

The X-ray absorption near edge structure (XANES) and the Fourier-transformed extended X-ray absorption fine structure (FT-EXAFS) at the Mo K-edge of the reference materials, sulfided supported, and unsupported catalysts are shown in
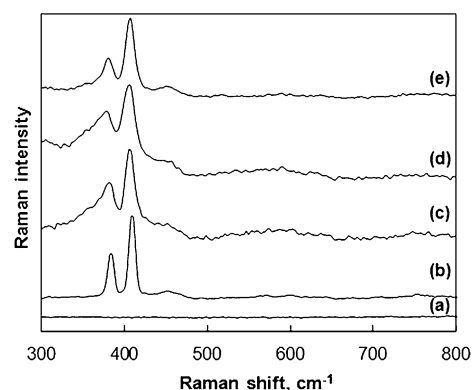

Figure 4. Raman spectra of the reference materials a) Ni_3S_2 and b) MoS_2 and the sulfided catalysts c) $MoS_2/\gamma-Al_2O_3$, d) $Ni-MoS_2/\gamma-Al_2O_3$, and e) $Ni-MoS_2/$ unsupported.

Figure 5. The absorption edge energy and the local environment around Mo of the sulfided catalysts and the MoS_2 reference material were almost identical. In accordance with the well-known layered sandwich structure of 2H-MoS_2, the first contribution at around 1.9 Å (not phase corrected) can refer to Mo—S and the second one at 2.8 Å (not phase corrected) to Mo—Mo distances.[19] Interestingly, the Mo—S contribution was more intense for both Ni-containing catalysts, whereas the Mo—Mo signal intensity was the highest for the bulk MoS_2 reference sample.

The XANES and FT-EXAFS data at the Ni K-edge of the reference materials, sulfided supported, and unsupported catalysts are presented in Figure 6. At around 8332 eV, a small pre-edge was found in the XANES, typical for tetrahedrally or pentagonally coordinated Ni species (Figure 6 B). The absorption edge energy of $Ni-MoS_2/\gamma-Al_2O_3$ was 8339 eV, whereas an edge energy of 8338 eV was observed for $Ni-MoS_2/unsupported$ and the Ni_3S_2 reference material. The features in the FT-EXAFS at the Ni K-edge were similar to those found in the bulk Ni_3S_2 reference material that has a trigonal space group ($R32$), in which Ni is tetrahedrally coordinated by four S atoms with an interatomic distance of approximately 2.3 Å. The second coordination shell, defined by four Ni atoms, is located at approximately 2.5 Å.[20] This closely spaced environment is reflected in the intense and broad backscatter signal in the FT-EXAFS of the Ni_3S_2 reference material. The observed contributions of the catalysts showed, however, much lower intensities and were shifted to shorter distances compared to that of Ni_3S_2. Moreover, the more distant Ni—Ni contribution of Ni_3S_2 at approximately 3.7 Å (not phase corrected) was almost absent in the catalysts.

Linear combination fitting (LCF) as well as the use of difference spectra were applied to explore the data by using the XANES of the reference bulk ma-
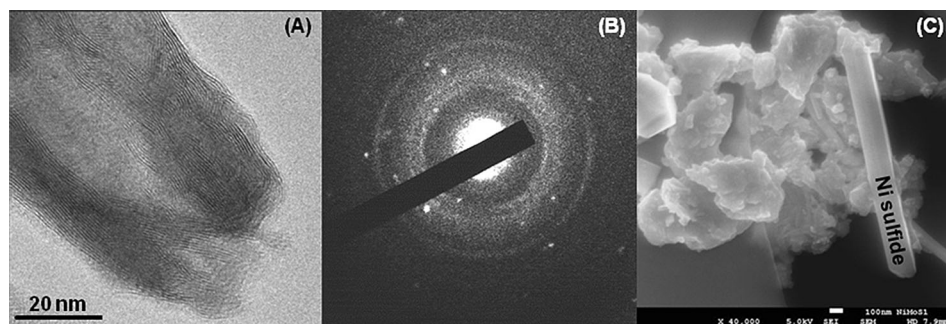
Figure 3. A) TEM image, B) selected-area diffractogram, and C) HR-SEM image of $Ni-MoS_2/unsupported$. The rings in (B) and stacked particles in (C) are identified as the MoS_2 phase, whereas the dots in (B) and the needles in (C) belong to Ni_9S_8 and Ni_3S_4. Scale bars = A) 20 nm, C) 100 nm.
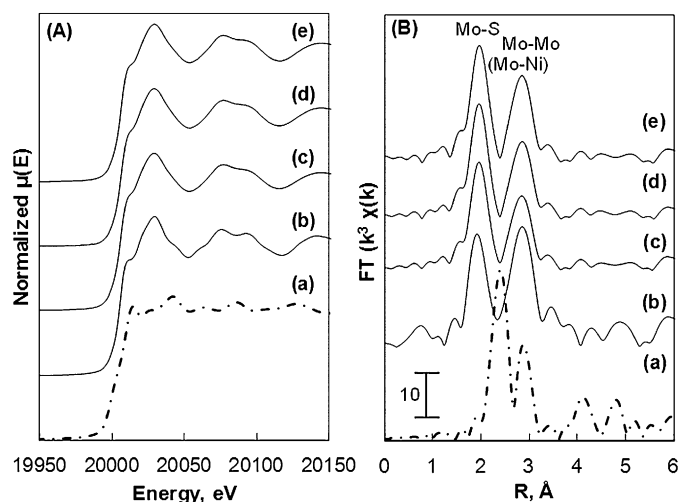
Figure 5. A) Mo K-edge XANES and B) FT of k^3-weighted EXAFS of references and sulfide catalysts: a) Mo foil, b) MoS_2, c) Mo/γ-Al_2O_3, d) Ni-MoS_2/γ-Al_2O_3, and e) Ni-MoS_2/unsupported.
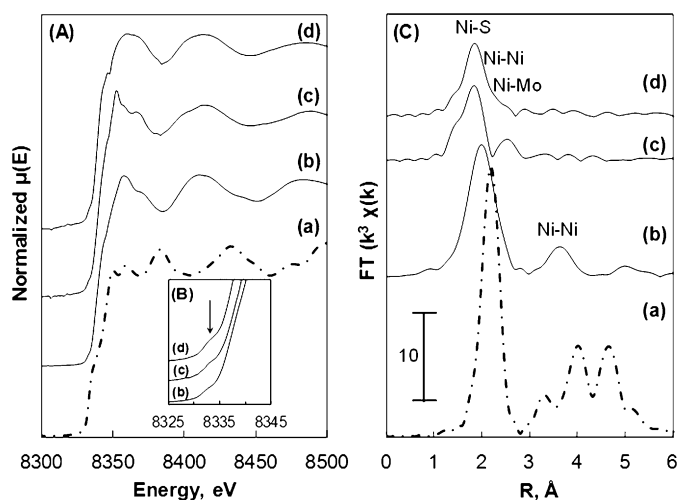
Figure 6. A) Ni K-edge XANES, B) pre-edge region, and C) FT of k^3-weighted EXAFS of references and sulfide catalysts: a) Ni foil, b) Ni_3S_2, c) Ni-MoS_2/γ-Al_2O_3, and d) Ni-MoS_2/unsupported.

terials MoS_2 and Ni_3S_2 and the oxidic precursors (the most important results for this analysis are provided in the Supporting Information in Table S4 and Figure S10). Analysis of the difference spectra shows that the XANES of the catalysts cannot be reproduced by using only sulfide references. Therefore, the XANES of the oxidic precursor were used in addition to the references for the LCF. The XANES of MoS_2/γ-Al_2O_3 at the Mo K-edge can be described with a contribution of 93% of the XANES of the MoS_2 reference and a contribution of 7% of the Mo/γ-Al_2O_3 catalyst precursor XANES.

The XANES of Ni-MoS_2/γ-Al_2O_3 is reproduced with 94% contribution of MoS_2 and 6% contribution of the oxidic precursor at the Mo K-edge and 85% contribution of Ni_3S_2 and 15% contribution of the oxide precursor at the Ni-edge. The LCF of the XANES of Ni-MoS_2/unsupported needs 98% MoS_2 at the Mo K-edge and 95% Ni_3S_2 at the Ni K-edge to reproduce the experimental XANES, and the difference corresponds to the oxidic precursor.

The approach of combining the XANES of sulfide references and oxidic precursors allowed the precise modeling of the XANES measured for the sulfided catalysts. However, analysis of the difference spectra between the experimental XANES and the model spectra generated by LCF indicates that other phases (most likely crystallographic structures with neighboring Mo and Ni) also contribute to the XANES of the catalysts, especially at the Ni K-edge.

Consequently, Mo–Ni and Ni–Mo scattering contributions were added for the multi-edge fit procedure of the EXAFS data to obtain the structural parameters of the catalysts. The structure of the reference material Ni_3S_2 is described by two Ni–S and two Ni–Ni contributions, whereas for the Ni-MoS_2/γ-Al_2O_3 catalyst these paths were not distinguishable and only a single path was used to fit the Ni–S and Ni–Ni contributions. Additionally, to describe the EXAFS data at the Ni K-edge, a Ni–O path at 2.0 Å and a Ni–Ni path at 3.0 Å are necessary to describe the Ni–O interaction. In the case of Ni-MoS_2/unsupport-

ed, this oxidic Ni–Ni contribution did not improve the fit. For both Ni-containing catalysts, the overall multi-edge fit is improved by approximately 20% if Mo–Ni (Ni–Mo) contributions are added. The best fit for the Mo–S, Mo–Ni, and Mo–Mo contributions is presented in Table 2 and that for the Ni–S, Ni–Ni, and Ni–Mo contributions is presented in Table 3 (the corresponding fitted EXAFS data are provided in Figures S11 and S12).

An almost complete first coordination shell with a coordination number $N_{Mo–S} = 5.7$ (at 2.41 Å) and lower $N_{Mo–Mo} = 4.3$ (at 3.17 Å) were found in the MoS_2/γ-Al_2O_3 catalyst compared to the bulk MoS_2, with $N_{Mo–S} = 5.8$ (at 2.40 Å) and $N_{Mo–Mo} = 6$ (at 3.16 Å). In the Ni-promoted catalysts, the coordination numbers were $N_{Mo–S} = 6.6$ and $N_{Mo–Mo} = 4.1$ for Ni-MoS_2/γ-Al_2O_3 and $N_{Mo–S} = 6.4$ and $N_{Mo–Mo} = 4.4$ for Ni-MoS_2/unsupported. Moreover, a new Mo–Ni contribution was found with a coordination number of $N_{Mo–Ni} = 0.2$ (at 2.79 Å) in the supported catalyst and $N_{Mo–Ni} = 0.3$ (at 2.66 Å) in Ni-MoS_2/unsupported. The Mo–Mo contribution overlaps with the Mo–Ni contribution, therefore, the latter is not directly observable in the FT-EXAFS data (Figure 5).

The first coordination shell of Ni in Ni-MoS_2/γ-Al_2O_3 consists of an O atom with $N_{Ni–O} = 0.9$ (at 1.94 Å), and in Ni-MoS_2/unsupported $N_{Ni–O} = 0.3$ (at 1.94 Å). If we consider that nickel oxide species have an octahedral coordination ($N_{Ni–O} = 6$), these coordination numbers can be related to concentrations of nickel oxide species of 15% in Ni-MoS_2/γ-Al_2O_3 and 5% in Ni-MoS_2/unsupported, which is in line with the LCF analysis described above. The high concentration of nickel oxide species in Ni-MoS_2/γ-Al_2O_3 can be attributed to spinel $NiAl_2O_4$ because of the presence of Ni atoms at 3.02 Å with $N_{Ni–Ni} = 0.5$.

The second coordination shell in Ni-MoS_2/γ-Al_2O_3 consist of S atoms with a distance of 2.24 Å, which is between the values of the two Ni–S coordination shells in the reference Ni_3S_2 material (2.23 and 2.27 Å). As a result of the smaller particle size of the catalysts these two shells could not be separated. The

Table 2. Best-fit results for k^3-weighted EXAFS data of the sulfided catalysts at the Mo K-edge in k space. N: coordination number, r: distance, E_0: inner potential, σ^2: Debye–Waller factor, (absolute error).

Catalyst	Shell	r [Å]	N	σ^2 [Å²]	E_0 [eV]
MoS₂/γ-Al₂O₃	Mo—S	2.41	5.7	0.0028	6.12
(R=0.0017)		(0.01)	(0.3)	(0.0003)	(1.25)
	Mo—Mo	3.17	4.3	0.0028	3.62
		(0.01)	(0.3)	(0.0003)	(1.25)
Ni-MoS₂/γ-Al₂O₃	Mo—S	2.41	6.6	0.0031	1.57
(R=0.0012)		(0.01)	(0.2)	(0.0001)	(0.28)
	Mo—Ni	2.79	0.2	0.0024	1.57
		(0.03)	(0.1)	(0.0022)	(0.28)
	Mo—Mo	3.17	4.1	0.0023	1.57
		(0.01)	(0.2)	(0.0002)	(0.28)
Ni-MoS₂/unsupported	Mo—S	2.40	6.4	0.0028	0.66
(R=0.0014)		(0.01)	(0.2)	(0.0001)	(0.28)
	Mo—Ni	2.66	0.3	0.0020	0.66
		(0.02)	(0.1)	(0.0018)	(0.28)
	Mo—Mo	3.17	4.4	0.0019	0.66
		(0.01)	(0.2)	(0.0001)	(0.28)
MoS₂	Mo—S	2.40	5.8	0.0019	−0.50
(R=0.0093)		(0.02)	(0.6)	(0.0007)	(4.47)
	Mo—Mo	3.16	6.0	0.0014	−0.50
		(0.02)	(0.6)	(0.0005)	(4.47)

Table 3. Best-fit results for k^3-weighted EXAFS data of the sulfided catalysts at the Ni K-edge in k space. N: coordination number, r: distance, E_0: inner potential, σ^2: Debye–Waller factor, (absolute error).

Catalyst	Shell	r [Å]	N	σ^2 [Å²]	E_0 [eV]
Ni-MoS₂/γ-Al₂O₃	Ni—O	1.94	0.9	0.0000	1.77
(R=0.0012)		(0.01)	(0.2)	(0.0001)	(0.92)
	Ni—S	2.24	2.4	0.0027	1.77
		(0.01)	(0.2)	(0.0005)	(0.92)
	Ni—Ni	2.59	1.0	0.0099	1.77
		(0.03)	(0.4)	(0.0035)	(0.92)
	Ni—Mo	2.79	0.2	0.0024	1.77
		(0.03)	(0.1)	(0.0022)	(0.92)
	Ni—Ni	3.02	0.5	0.0049	1.77
		(0.04)	(0.2)	(0.0042)	(0.92)
Ni-MoS₂/unsupported	Ni—O	1.94	0.3	0.0015	2.82
(R=0.0014)		(0.06)	(0.1)	(0.0007)	(1.24)
	Ni—S	2.20	1.2	0.0000	2.82
		(0.01)	(0.2)	(0.0001)	(1.24)
	Ni—S	2.31	1.5	0.0011	2.82
		(0.02)	(0.2)	(0.0009)	(1.24)
	Ni—Ni	2.59	1.5	0.0064	2.82
		(0.02)	(0.4)	(0.0018)	(1.24)
	Ni—Mo	2.66	0.3	0.0020	2.82
		(0.02)	(0.1)	(0.0018)	(1.24)
Ni₃S₂[a]	Ni—S	2.23	2.0	–	–
	Ni—S	2.27	2.0	–	–
	Ni—Ni	2.47	2.0	–	–
	Ni—Ni	2.49	2.0	–	–

[a] The structural parameters of Ni₃S₂ correspond to the crystallographic data in ICSD # 27521.[20]

third coordination shell consists of Ni atoms and shifts to longer distances and lower total coordination numbers (Ni—Ni

and Ni—S) for Ni-MoS₂/γ-Al₂O₃ compared to Ni₃S₂. In Ni-MoS₂/unsupported, two S coordination shells were observed. The first at 2.20 Å with N_{Ni-S} = 1.2 was shifted to a shorter distance and the second at 2.31 Å with N_{Ni-S} = 1.5 to a longer distance compared to the Ni₃S₂ reference material. The Ni—Ni backscattering was found at the same distance as that in Ni-MoS₂/γ-Al₂O₃ with a higher coordination number of 1.5. Similar to Ni-MoS₂/γ-Al₂O₃, the coordination number of the Ni—S contribution in Ni-MoS₂/unsupported was lower than that in Ni₃S₂. Moreover, in both Ni-containing catalysts an additional Ni—Mo contribution was found with N_{Ni-Mo} = 0.2 at 2.79 Å and N_{Ni-Mo} = 0.3 at 2.66 Å in the supported and unsupported catalysts, respectively.

## The HDN of quinoline as a space-time-dependent experiment

The HDN reaction network of quinoline (Q) is presented in Scheme 1. The reaction proceeds by the hydrogenation of the pyridinic ring to form 1,2,3,4-tetrahydroquinoline (14THQ) or by the hydrogenation of the aromatic ring to 5,6,7,8-tetrahydroquinoline (58THQ). Further hydrogenation of 14THQ or 58THQ forms decahydroquinoline (DHQ). The reaction can then continue through two routes, that is, the ring opening of 14THQ to o-propylaniline (OPA) and of DHQ to propylcyclohexylamine (PCHA). OPA is converted to propylbenzene (PB) by direct denitrogenation, whereas N is removed from PCHA to form propylcyclohexene (PCHE).

According to the detailed analysis in Ref. [21], the hydrogenation of the phenyl ring in OPA is the rate-determining step in the sequence Q→14THQ (by hydrogenation)→OPA (by ring opening)→PCHA (by denitrogenation). In the sequence DHQ→PCHA (by ring opening)→PCHE (by denitrogenation)→propylcyclohexane (PCH; by hydrogenation), the C(sp³)—N bond cleavage in the primary amine (PCHA) is fast, and the C(sp³)—N bond cleavage in DHQ is the rate-limiting step.

Q HDN conversion showed a nonlinear dependence as a function of the space time at 370 °C (Figure 7). At first the rate of N removal is negligible, but as soon as a significant concentration of DHQ is reached the rate increased (Figures 8–10). The HDN activity increased in the order MoS₂/γ-Al₂O₃ < Ni-MoS₂/unsupported < Ni-MoS₂/γ-Al₂O₃. The initially low rate is a direct consequence of the inhibition by 14THQ that is adsorbed more strongly on the catalyst surface than Q.[22]

The effect of the space time on the product distribution is shown in Figures 8–10. At first Q was converted quickly to 14THQ to reach the equilibrium (Figure S13). Furthermore, over the whole space time studied, DHQ and 58THQ were in thermodynamic equilibrium (Figure S13). Therefore, (Q+14THQ) and (DHQ+58THQ) were combined for further analysis. The primary products observed that exhibited linearly increasing yields at low space time values were (58THQ+DHQ) and OPA. Further conversion of the secondary products, PCHA and PCHE, led to the final products, PB and PCH. Three isomers of PCHE were detected and combined for further analysis: 1-propylcyclohexene (with the highest yield related to its high stability), 3-propylcyclohexene, and propylidene cyclohexane.
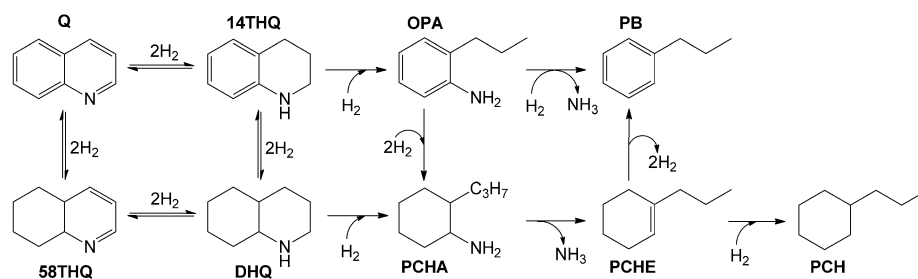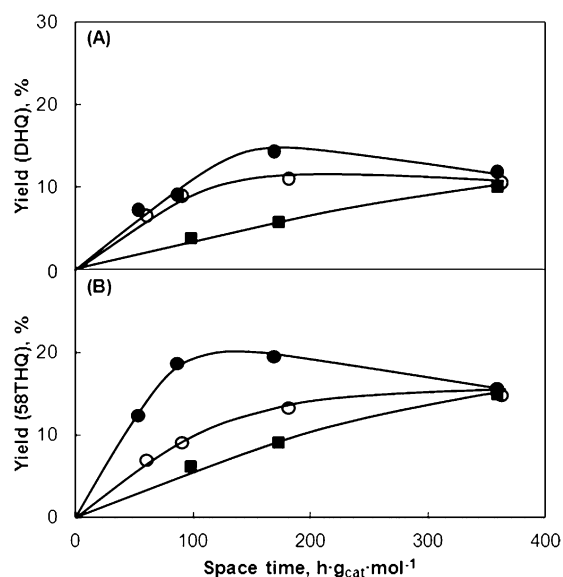
Scheme 1. HDN reaction network of Q. Abbreviations: 14THQ, 1,2,3,4-tetrahydroquinoline; 58THQ, 5,6,7,8-tetrahydroquinoline; DHQ, decahydroquinoline; OPA, *o*-propylaniline; PCHA, propylcyclohexylamine; PB, propylbenzene; PCHE, propylcyclohexene; PCH, propylcyclohexane.

rate of 14THQ ring opening to form OPA increased in the order Ni-MoS$_2$/unsupported < MoS$_2$/γ-Al$_2$O$_3$ < Ni-MoS$_2$/γ-Al$_2$O$_3$. This ring opening of 14THQ by C(sp^3)—N bond cleavage to form OPA, has a lower reaction rate compared to the parallel hydrogenation of the benzoic ring to form DHQ (Figures 8A and 9A). Further hydrogenation of OPA to PCHA is negligible as long as Q, 14THQ,
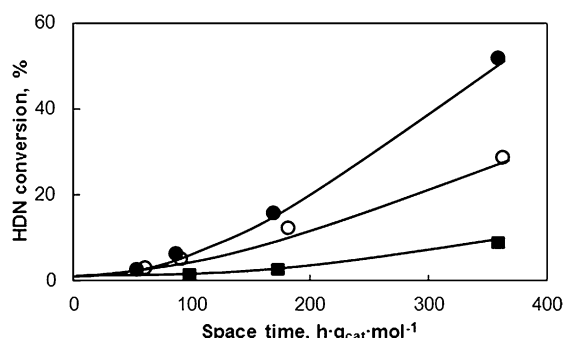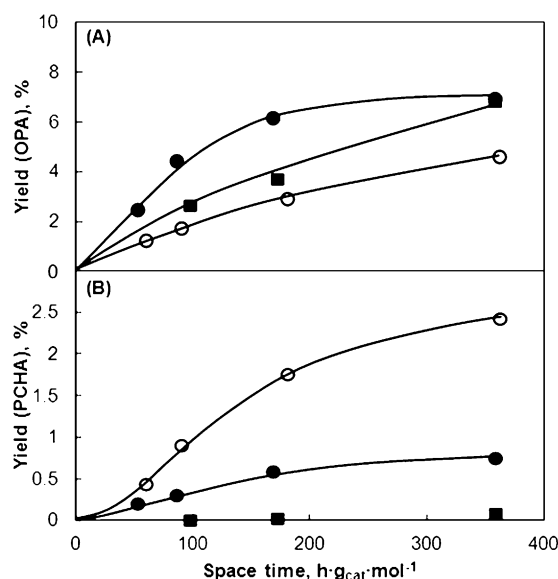

Figure 7. Quinoline HDN conversion as a function of the space time at 370 °C on MoS$_2$/γ-Al$_2$O$_3$ (■), Ni-MoS$_2$/γ-Al$_2$O$_3$ (●), and Ni-MoS$_2$/unsupported (○).

Figure 9. Yield of A) OPA and B) PCHA as a function of the space time at 370 °C on MoS$_2$/γ-Al$_2$O$_3$ (■), Ni-MoS$_2$/γ-Al$_2$O$_3$ (●), and Ni-MoS$_2$/unsupported (○).

Figure 8. Yield of A) DHQ and B) 58THQ as a function of the space time at 370 °C on MoS$_2$/γ-Al$_2$O$_3$ (■), Ni-MoS$_2$/γ-Al$_2$O$_3$ (●), and Ni-MoS$_2$/unsupported (○).

The rate of DHQ formation, by hydrogenation of the benzoic ring in 14THQ, and the rate of 58THQ formation, by hydrogenation of the benzoic ring in quinoline, was the highest on Ni-MoS$_2$/γ-Al$_2$O$_3$ and the lowest on MoS$_2$/γ-Al$_2$O$_3$ (Figure 8). The

58THQ, and DHQ are present because of their strong adsorption on the catalyst surface.[23,24]

The other ring-opening intermediate, PCHA (from DHQ), was either not detected or the yield was < 1 % on Ni-MoS$_2$/γ-Al$_2$O$_3$ and < 2.5 % on Ni-MoS$_2$/unsupported catalyst. The rate of N removal from PCHA to PCHE, which is hydrogenated to PCH, increased in the order MoS$_2$/γ-Al$_2$O$_3$ < Ni-MoS$_2$/unsupported < Ni-MoS$_2$/γ-Al$_2$O$_3$.

In parallel to the HDN of Q, the conversion of DBT was also followed (Figure 11). The Ni-promoted catalysts exhibited higher HDS conversion rates, for instance, at the space time of 100 h g$_{cat}$ mol^{-1}, the DBT conversion was 12 % on MoS$_2$/γ-Al$_2$O$_3$, 45 % on Ni-MoS$_2$/unsupported, and 90 % on Ni-MoS$_2$/γ-Al$_2$O$_3$. The product distribution (Figure 11 B and C) indicated that the main route for DBT conversion was direct desulfurization, of which biphenyl (BPh) was the only product. Low yields of phenylcyclohexane (PhCH) were detected over the whole space time: < 2 % on MoS$_2$/γ-Al$_2$O$_3$, < 8 % on Ni-MoS$_2$/γ-Al$_2$O$_3$ (and none with Ni-MoS$_2$/unsupported).
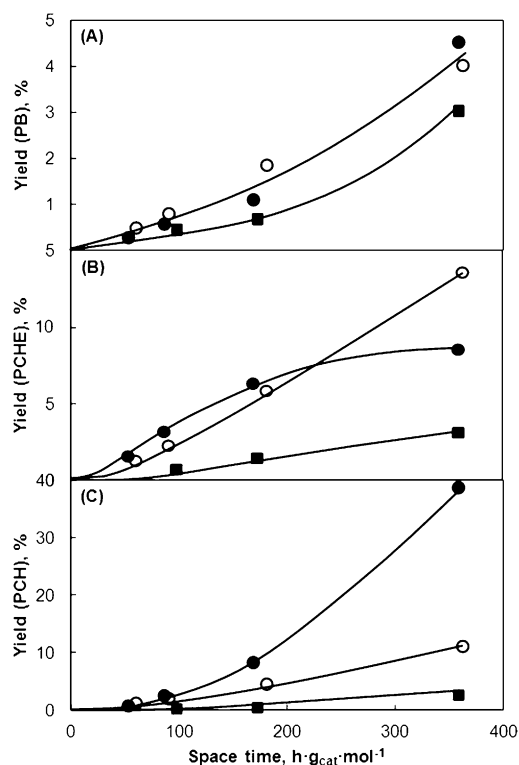
Figure 10. Yield of A) PB, B) PCHE, and C) PCH as a function of the space time at 370 °C on MoS₂/γ-Al₂O₃ (■), Ni-MoS₂/γ-Al₂O₃ (●), and Ni-MoS₂/ unsupported (○).

Figure 11. A) DBT conversion and yields of B) PhCH and C) BPh as a function of space time in the parallel reaction with the HDN of Q at 370 °C performed on MoS₂/γ-Al₂O₃ (■), Ni-MoS₂/γ-Al₂O₃ (●), and Ni-MoS₂/unsupported (○).

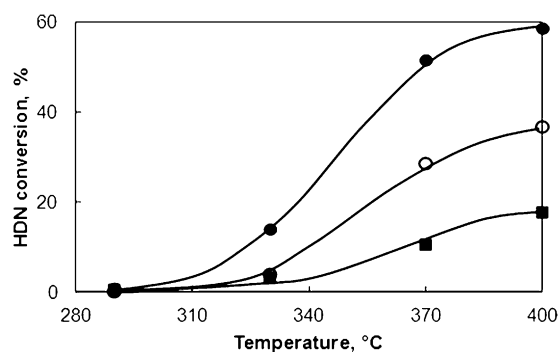## The temperature dependence of quinoline HDN

The rate of N removal strongly depends on the reaction temperature and exhibits an S-shaped increase (Figure 12). At 290 °C, only hydrogenation to 14THQ and DHQ occurs, whereas at 330 °C the first ring-opening and N-free products are observed (Figures 13–15). A further temperature increase to 370 °C accelerates the rate of N removal. However, above 370 °C the HDN rate increases only slightly. This modest increase in N removal originates from the Q–14THQ thermodynamic equilibrium, which shifts towards Q at increasing temperatures.[25]

The product distribution shifted with increasing reaction temperature from hydrogenated products through ring-opening products towards N-free products. The yield of 58THQ (the product of the benzoic ring hydrogenation) on the Ni-MoS₂/γ-Al₂O₃ catalyst was the maximum at 380 °C (20%), whereas Ni-MoS₂/unsupported and MoS₂/γ-Al₂O₃ showed an increase of the 58THQ yield with increasing temperature that reached 30% at 400 °C (Figure 13 B). DHQ showed a maximum yield at around 330 °C on Ni-MoS₂/γ-Al₂O₃ (27%) and Ni-MoS₂/unsupported (20%), whereas on MoS₂/γ-Al₂O₃ the maximum appeared at around 350 °C (12%; Figure 13 A). Although the OPA yield increased with increasing temperature, the PCHA yield exhibited a maximum at around 330 °C (1.5%) on Ni-MoS₂/γ-Al₂O₃ and at around 350 °C (3.5%) on Ni-MoS₂/unsupported (Figure 14 A and B).

The conversion to N-free products began at 330 °C. The PB yield increased with temperature to reach 3.3, 8.5, and 12.5%

Figure 12. Q HDN conversion as a function of temperature at the space time of 350 h g$_{cat}$ mol⁻¹ on MoS₂/γ-Al₂O₃ (■), Ni-MoS₂/γ-Al₂O₃ (●), and Ni-MoS₂/unsupported (○).

at 400 °C on MoS₂/γ-Al₂O₃, Ni-MoS₂/unsupported, and Ni-MoS₂/ γ-Al₂O₃, respectively (Figure 15 A). PCHE exhibited a maximum yield at 370 °C on Ni-MoS₂/γ-Al₂O₃ (8.5%), whereas an S-shaped dependence was observed on MoS₂/γ-Al₂O₃ and Ni-MoS₂/unsupported, and the yield reached 7 and 17% respectively, at 400 °C (Figure 15 B). The PCH yield increased with increasing temperature on the studied catalysts and reached the maximum of 8.1, 10, and 41.6% on MoS₂/γ-Al₂O₃, Ni-MoS₂/unsupported, and Ni-MoS₂/γ-Al₂O₃, respectively (Figure 15 C).

The conversion of DBT was also followed (Figure 16). The DBT conversion increased from 5 (at 290 °C) to 43% (at 400 °C)
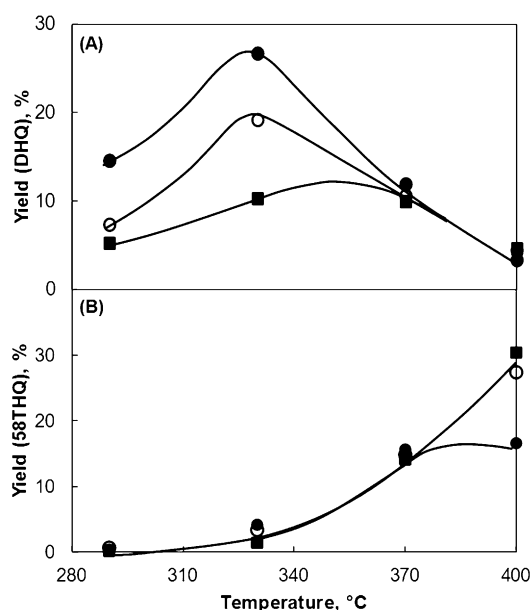
Figure 13. Yield of A) DHQ and B) 58THQ as a function of the temperature at the space time of 350 h g_{cat} mol^{-1} on MoS$_2$/γ-Al$_2$O$_3$ (■), Ni-MoS$_2$/γ-Al$_2$O$_3$ (●), and Ni-MoS$_2$/unsupported (○).
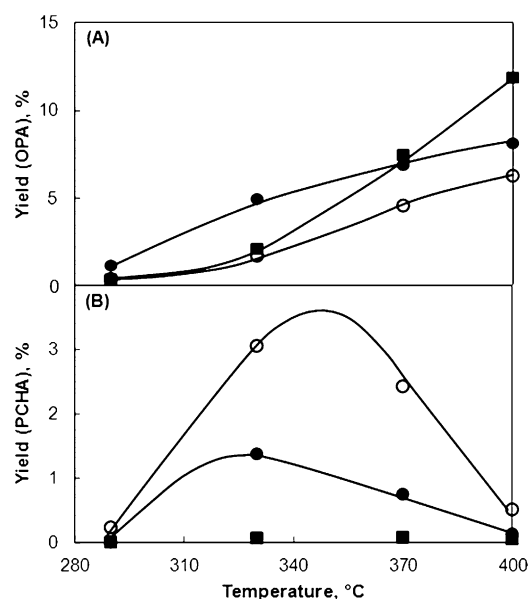
Figure 14. Yield of A) OPA and B) PCHA as a function of the temperature at the space time of 350 h g_{cat} mol^{-1} on MoS$_2$/γ-Al$_2$O$_3$ (■), Ni-MoS$_2$/γ-Al$_2$O$_3$ (●), and Ni-MoS$_2$/unsupported (○).

on MoS$_2$/γ-Al$_2$O$_3$ and from 32 (at 290 °C) to 90 % (at 400 °C) on Ni-MoS$_2$/unsupported. On Ni-MoS$_2$/γ-Al$_2$O$_3$, the DBT conversion reached 100 % at 330 °C. The product distribution (Figure 16 B and C) indicated that the yield of the hydrogenated product, PhCH, increased with the increase of the reaction temperature to reach 4 % on MoS$_2$/γ-Al$_2$O$_3$, 7 % on Ni-MoS$_2$/unsupported, and 12 % on Ni-MoS$_2$/γ-Al$_2$O$_3$. BPh was the main product in all cases. On MoS$_2$/γ-Al$_2$O$_3$, the BPh yield increased continuously up to 40 % at 400 °C. On Ni-MoS$_2$/unsupported, the yield
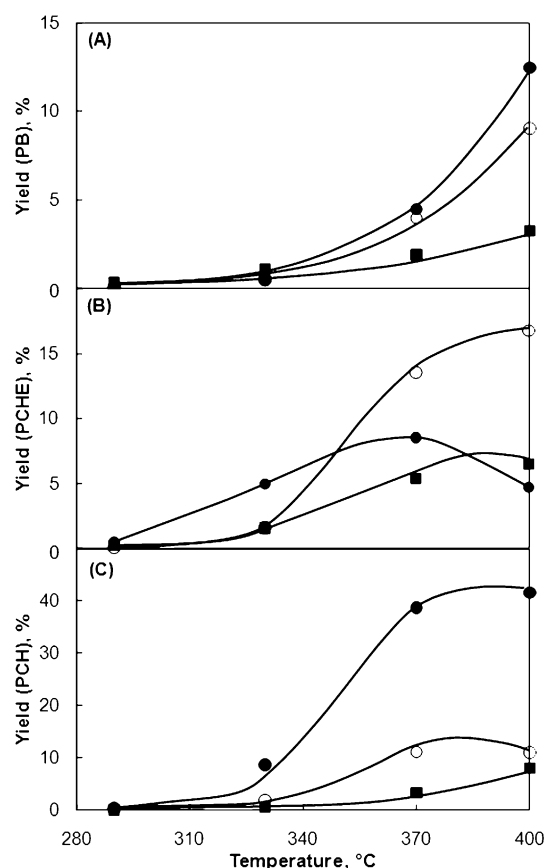
Figure 15. Yield of A) PB, B) PCHE, and C) PCH as a function of the temperature at the space time of 350 h g_{cat} mol^{-1} on MoS$_2$/γ-Al$_2$O$_3$ (■), Ni-MoS$_2$/γ-Al$_2$O$_3$ (●), and Ni-MoS$_2$/unsupported (○).

reached 80 % at 370 °C and remained constant, whereas on Ni-MoS$_2$/γ-Al$_2$O$_3$ the BPh yield increased to ~100 % at 320 °C and decreased at higher temperatures.

Discussion

Catalyst characterization: Oxide precursors and their sulfidation

The Mo concentration of 2.5 Mo atoms nm^{-2} in the supported materials is far below the monolayer concentration of γ-Al$_2$O$_3$ (4.6–5 atoms nm^{-2}).[26] Accordingly, the XRD patterns do not exhibit reflections of a crystalline Mo-containing phase (Figure S1 d and e), and the Raman spectra indicate the existence of well-dispersed polymolybdate species[27–31] (Figure S3 A,e–A,f). The presence of the characteristic pre-edge peak in the Mo K-edge XANES (at 20 005 eV) indicates that Mo is present in a distorted octahedral coordination geometry (Figure S4 A).[31, 32]

After Ni promotion, the Raman band that corresponds to the terminal Mo≡O symmetric stretching vibration is shifted from 961 cm^{-1} in Mo/γ-Al$_2$O$_3$ to 947 cm^{-1} in NiMo/γ-Al$_2$O$_3$. The shoulder at 860 cm^{-1} assigned to the asymmetric stretching vibration of the Mo—O—Mo bridging bond becomes more intense, which suggests that Ni increases the aggregation of the
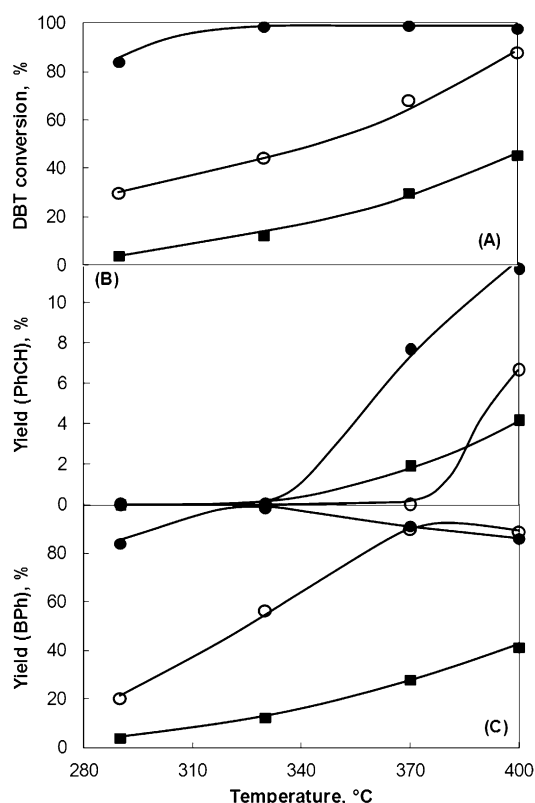
Figure 16. A) DBT conversion, B) yield of PhCH, and C) yield of BPh as a function of temperature in the parallel reaction with the HDN of Q at the space time of 350 h g_{cat} mol^{-1} performed on MoS$_2$/γ-Al$_2$O$_3$ (■), Ni-MoS$_2$/γ-Al$_2$O$_3$ (●), and Ni-MoS$_2$/unsupported (○).

Mo species, that is, Ni leads to a higher oligomerization degree of molybdenum oxide species.[33,34] This is confirmed by the analysis of the UV/Vis spectra, which shows that the number of nearest Mo neighbors increased with the addition of Ni. The creation of these new Mo–O–Mo bonds may occur from terminal Mo=O groups or by breaking Al–O–Mo bonds with the support.

The NiMo/unsupported oxide catalyst precursor presents a mixture of nickel molybdate (NiMoO$_4$), and ammonium nickel molybdate ((NH$_4$)HNi$_2$(OH)$_2$(MoO$_4$)$_2$; see XRD patterns in Figure S1 f and the Raman spectrum in Figure S3 A,f). The Ni-to-Mo metal ratio of 1.07 (Table 1) matches well with the stoichiometry of the identified compounds. The average number of nearest Mo neighbors determined by UV/Vis and X-ray absorption spectroscopy confirms the presence of molybdates. The XANES at the Mo K-edge showed pre-edge features characteristic of tetrahedral Mo species (Figure S4 A, g), and the UV/Vis spectra (Figure S3 B,f) exhibited two features assigned to octahedrally coordinated Ni^{2+} (ammonium nickel molybdate) and tetrahedrally coordinated Ni^{2+} (nickel molybdate). The ammonium nickel molybdate species in NiMo/unsupported can, therefore, be described as a layered structure of distorted Ni octahedra and Mo tetrahedra that form layers in the *c* direction.[35]

The temperature-programmed sulfidation (TPS) of both supported Mo/γ-Al$_2$O$_3$ and NiMo/γ-Al$_2$O$_3$ oxide precursors showed

a profile with three sections.[15] In the low-temperature region O is substituted by S, as seen by the H$_2$S consumption in the TPS curve and the decrease of the shortest Mo–O bond coupled with the formation of a new Mo–S contribution shown in the FT-EXAFS (Figure S9). The terminal Mo=O bonds are the most reactive in the polymolybdate-like structure and, therefore, are among the first to form oxysulfide species.[35,36] In the second section, Mo is reduced from Mo^{6+} to Mo^{4+}, indicated by the H$_2$S release in the TPS profiles and the disappearance of the pre-edge feature in the XANES (Figure S8). The reduction temperature is shifted from 225 (Mo/γ-Al$_2$O$_3$) to 205 °C (NiMo/γ-Al$_2$O$_3$) because of the presence of Ni,[15] which induces a weaker interaction of the oxide precursor with the support. The last region is characterized by further H$_2$S consumption and the formation of new Mo–Mo contributions at a longer distance than that in the precursors, which indicates further conversion to the final MoS$_2$/γ-Al$_2$O$_3$ and Ni-MoS$_2$/γ-Al$_2$O$_3$. The TPS profile of NiMo/unsupported exhibited a continuous H$_2$S consumption over the whole temperature range. H$_2$S release was not observed, however, the reduction to Mo^{4+} in (NH$_4$)HNi$_2$(OH)$_2$(MoO$_4$)$_2$ and NiMoO$_4$ occurs between 270 and 305 °C as deduced by XANES data (Figures S8 and S9).

Catalyst characterization: Active phases present in the sulfide catalysts

MoS$_2$ is present in S–Mo–S sandwiched structures (MoS$_2$ slabs), in which S atoms coordinate Mo to form trigonal prisms. The stacking of these structures, stabilized by van der Waals interactions, leads to laminar assemblies. The support stabilizes MoS$_2$ with a relatively small number of layers (low stacking degree). In contrast to the MoS$_2$ phase, the morphology of the supported, Ni- or Co-promoted MoS$_2$ phase is controversial. Several models of the active phases have been proposed to explain the synergy between (W)Mo and (Ni)Co (e.g., Ref. [37]). At present, variants of the Co–Mo–S model, proposed originally by Topsøe et al.,[38] are widely accepted. This model suggests that Mo cations are substituted by Ni or Co at the edge position of the MoS$_2$ slabs. Strong evidence has been reported for this model, which includes EXAFS data,[39,40] DFT calculations,[41] and STM.[42,43]

The characterization results of the studied alumina-supported catalysts show that the MoS$_2$ slabs are well dispersed on alumina (XRD and TEM, Figures 1–3) and that the bulk and surface structure of MoS$_2$/γ-Al$_2$O$_3$ and Ni-MoS$_2$/γ-Al$_2$O$_3$ correspond to well-defined MoS$_2$. Indications of minority oxide species during the LCF analysis of the XANES data point to a very low concentration of Mo oxide species, as Mo–O contributions were not needed to fit the EXAFS data of the sulfide catalysts (Table 2). The only oxide species identified in the sulfided catalysts is a minority concentration of spinel NiAl$_2$O$_4$, whereas most of the Ni is present in sulfide phases. The presence of a Ni–Ni distance of 2.59 Å in the EXAFS, however, points to the formation of segregated Ni sulfides (Table 3). These Ni sulfides have to be very dispersed as they show only a low coordination number for the Ni–Ni contributions compared to Ni$_3$S$_2$, and none of these phases were identified by XRD or TEM anal-

ysis. The Mo–Ni contribution indicates the formation of a Ni–Mo–S phase, which dominates the performance (vide infra). The Mo–Ni coordination number of 0.2 is smaller than that generally reported for Ni–Mo–S,[19,44] however, the Ni–S and Ni–Mo distances match very well with the millerite-type structure proposed for this phase.[45] The difference in Mo–S coordination numbers for promoted and unpromoted catalysts (6.6 and 5.7, respectively) is also in line with the features expected for the NiMoS and MoS_2 phases. The higher coordination in the former indicates a higher degree of sulfidation for the Ni–Mo–S phase, which results from the weakened Mo–support interaction.[46] The characterization of the alumina-supported oxide precursors by Raman spectroscopy (Figure S3 B) and TPS[15] also confirms the weaker interaction of the Ni-promoted sulfides with the support. The very different catalytic performance also gives clear evidence for the existence of different phases in $MoS_2/\gamma\text{-}Al_2O_3$ and $Ni\text{-}MoS_2/\gamma\text{-}Al_2O_3$ (vide supra).

The phases present in $Ni\text{-}MoS_2$/unsupported must be discussed separately because the morphology of the unsupported species differs from the alumina-supported sulfides. The unsupported oxide precursor is a mixture of two well-defined crystalline species [identified by Raman spectroscopy, XRD, and TEM coupled with selected-area electron diffraction (SAD)], whereas highly dispersed polymolybdates were present on the supported counterparts. Thus, the sulfidation of the unsupported oxide precursor follows different kinetics during TPS compared to the supported materials. Clearly, the same reactions must occur for all three catalysts, that is, O—S exchange and the reduction of Mo^{6+}. For the unsupported catalyst, however, the segregation of Ni species to form Ni_3S_2 and the diffusion of the sulfidation and reduction agents to the core of the relatively large oxide crystals produces a continuous H_2S consumption, which does not allow differentiation between the stages of sulfidation. Nevertheless, the catalytic activity can be related only to sulfide phases because after sulfidation only a fraction of oxide species remains in the catalyst (LCF analysis). It has been shown by Mössbauer spectroscopy that Co—Mo—S-like phases occur at a similar molar ratio in unsupported and supported catalysts.[47,48]. However, the activity of the unsupported catalysts has been less stringently associated with the formation of the Co(Ni)MoS phase[49] than for supported catalysts, probably because the promoted structure may be different in unsupported sulfides than in supported ones. For instance, it has been proposed that a synergy between MoS_2 and Co sulfides replaces the decoration of MoS_2 by Co in bulk multimetallic sulfides.[50,51] By EXAFS fitting of $Ni\text{-}MoS_2$/unsupported, we found two distances for Ni–S contributions (2.20 and 2.31 Å) and a distance of 2.66 Å for Ni–Mo, which is smaller than that of the millerite-type structure claimed for $Ni\text{-}MoS_2/Al_2O_3$. In a recent study, Chianelli et al.[50] modeled the MoS_2–Co_9S_8 interface with Co in a cubic structure that follows the structure observed by EXAFS analysis (i.e., two Co–S distances and a Co–Mo distance shorter than expected in a millerite structure[52]), therefore, we speculate that in the unsupported catalyst the MoS_2 phase is also promoted by Ni_xS_y clusters in addition to the edge decoration with Ni atoms. The presence of bulk Ni_xS_y was also shown by XRD (Figure 1), HR-SEM

(Figure 3), and the Ni–Ni distance of 2.59 Å found by EXAFS analysis. Moreover, the coordination number of the Ni–Ni contribution (N_{Ni-Ni}) can be used as an indicator for the proportion of Ni present in Ni_xS_y clusters. Given that a higher value for N_{Ni-Ni} is observed for $Ni\text{-}MoS_2$/unsupported than for $Ni\text{-}MoS_2/Al_2O_3$, the amount of Ni_3S_2 is higher in $Ni\text{-}MoS_2$/unsupported.

It is plausible to assume that Ni_xS_y is formed if Ni reaches a certain concentration at the edges of MoS_2 particles. The Mo/Ni ratio is close to 1 in the catalyst, that is, the concentration of Ni is much higher than that required for the formation of the NiMoS phase.[7] Although it is difficult to determine the exact concentration and nature of the Ni_xS_y species present from the experimental results in this study, it is evident that the $Ni\text{-}MoS_2$/unsupported catalyst is a physical mixture of at least three sulfide phases, of which Ni-promoted MoS_2 structures dominate the catalytic behavior.
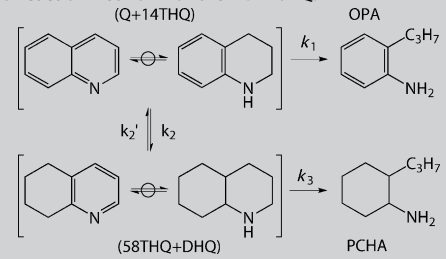
Unfortunately, it is not currently possible to differentiate strictly between the contributions of Ni_xS_y particles (probably also present in a wide range of sizes) and Ni atoms incorporated at the edges of the MoS_2 slabs. Regardless of the specific nature of the impact of Ni, the Ni–Mo interaction is observed clearly in the catalytic behavior. The unsupported catalyst is the second most active for HDN although the concentration of CUS determined for this catalyst is only half of that determined for $MoS_2/\gamma\text{-}Al_2O_3$ (from NO uptake experiments). Hence, the intrinsic activity of the unsupported catalyst is more similar to that of $Ni\text{-}MoS_2/\gamma\text{-}Al_2O_3$ than to that of $MoS_2/\gamma\text{-}Al_2O_3$. From the EXAFS analysis, Mo–Ni coordination numbers of 0.2 and 0.3 were obtained for $Ni\text{-}MoS_2/Al_2O_3$ and $Ni\text{-}MoS_2$/unsupported, which clearly indicate Mo–Ni interactions.

The HDN of quinoline

The first steps of the HDN reaction network can be simplified to the scheme shown in Table 4 because Q and 14THQ as well as 58THQ and DHQ equilibrate rapidly under the reaction conditions used (Figure S13). The overall (Q+14THQ) conversion, that is, (k_1+k_2), was fitted satisfactorily to a first-order kinetics with a correlation coefficient (R^2) above 0.99. The k_1/k_2 ratio was assumed to equal the initial OPA·$(58THQ+DHQ)^{-1}$ selectivity. Therefore, the absolute values of k_1 and k_2 were deduced from the overall conversion and the initial selectivity. The values of k_3 and k_2' were adjusted from the experimental concentration profiles of the products. The values of the subsequent steps of the HDN network are not quantitatively discussed because the strong adsorption of bicyclic compounds of Q may lead to inaccurate reaction rate constants. For a more detailed description see Ref. [21].

On all catalysts, the hydrogenation of (Q+14THQ) is faster than the dehydrogenation of (58THQ+DHQ). The k_2/k_2' ratios are in good agreement with the equilibrium constants among the bicyclic compounds.[21] However, the ring opening in DHQ is much faster than that of 14THQ, which is likely because of the lower intrinsic reactivity of 14THQ. Indeed, the ring opening of 14THQ may be a rate-limiting step in the whole HDN process together with the hydrogenation of OPA.[21] The activity of the catalysts (k_1+k_2) followed the same trend as that ob-

Table 4. Pseudo-first-order rate constants for the main reaction steps of a simplified reaction network for the HDN of Q.

Catalyst	$k_i \, [\mathrm{mol\,h^{-1}\,g_{cat}^{-1}}] \times 10^{-3}$			
	k_1	k_2	k_2'	k_3
MoS$_2$/γ-Al$_2$O$_3$	0.32	1.06	0.22	1.03
Ni-MoS$_2$/γ-Al$_2$O$_3$	0.64	4.96	0.94	3.30
Ni-MoS$_2$/unsupported	0.28	3.13	0.63	3.80

served for HDN conversion (Figure 7), that is, MoS$_2$/γ-Al$_2$O$_3$ < Ni-MoS$_2$/unsupported < Ni-MoS$_2$/γ-Al$_2$O$_3$. Interestingly, the (de)hydrogenation activity (k_2 and k_2') follows the same trend, whereas the rate of the ring-opening steps increased in the order Ni-MoS$_2$/unsupported ≤ MoS$_2$/γ-Al$_2$O$_3$ < Ni-MoS$_2$/γ-Al$_2$O$_3$ for 14THQ (k_1) and MoS$_2$/γ-Al$_2$O$_3$ < Ni-MoS$_2$/γ-Al$_2$O$_3$ ≤ Ni-MoS$_2$/unsupported for DHQ (k_3).

On the nature of the active sites

The specific geometric arrangement of the active sites in the MoS$_2$ and Ni-promoted phases remains inconclusive to date. The general agreement is that the edges of the MoS$_2$ slabs, decorated with Ni or not, are catalytically active. The adsorption of the reactants occurs through electron donation from heteroatoms or aromatic rings on CUS, that is, Mo or Ni atoms with Lewis acid character. Detailed descriptions of these interactions can be found in numerous reviews on the subject (e.g., Refs. [2, 53–56]). The basic sulfur anions are also claimed to play a fundamental role in the activity of the sulfide phase (probably also in combination with CUS) for H$_2$ activation.[21] After the dissociative adsorption of H$_2$ (or H$_2$S) on these sites, (S—S)$^{2-}$ dimers or S^{2-}—CUS pairs, —SH groups are created at the edges. These groups provide the H required for hydrogenation and hydrogenolysis. Furthermore, the —SH groups have been identified to have an acidic character in C(sp$_2$)—N bond scission mechanisms.[57,58] In general, the basal planes of the MoS$_2$ slabs are considered inactive. However, based on STM studies, Lauritsen et al.[38] proposed additional active sites located on the basal planes adjacent to the edges of MoS$_2$. These so-called brim sites exhibit a metal character (ability to donate and accept electrons) and are claimed to adsorb reactants and catalyze a hydrogenation step in the HDS of thiophene.

At this point we relate the activity results with the above-described potential sites in the catalysts. It has been shown that the promoted Ni-MoS$_2$/γ-Al$_2$O$_3$ catalyst is superior for N removal compared to its parent MoS$_2$/γ-Al$_2$O$_3$ catalyst in the whole temperature range (Figure 12). This observation is in line with

the assumption that Mo cations are substituted at the edge positions of the MoS$_2$ slabs upon addition of Ni to create new and more active catalytic sites for HDN.[1] However, it is important to note that Ni does not promote the removal of N from all N-containing compounds. The direct denitrogenation of OPA decreases with the incorporation of Ni to the MoS$_2$ slabs.[10,15] Thus, the active site for the DDN of OPA is related only to Mo-associated CUS. At the same time, the hydrogenation of the OPA phenyl ring is dramatically enhanced by Ni probably because of the promotion of brim sites.[15] Accordingly, the promoted Ni-MoS$_2$/γ-Al$_2$O$_3$ catalyst exhibits a higher hydrogenation rate than MoS$_2$/γ-Al$_2$O$_3$ (k_2 increases by a factor of five; Table 4).

If the reaction steps of Q HDN could be related to specific locations in the MoS$_2$ particles, one would expect that the absence of support and high stacking degree of the sulfides in Ni-MoS$_2$/unsupported would lead to a completely different catalytic performance compared to that of Ni-MoS$_2$/γ-Al$_2$O$_3$. However, the performance of Ni-MoS$_2$/unsupported is similar to that of Ni-MoS$_2$/γ-Al$_2$O$_3$. For instance, in the (de)hydrogenation steps the presence of Ni is more important than the presence of the support (k_2 and k_2' of Ni-containing catalysts are much higher than those of MoS$_2$/γ-Al$_2$O$_3$). The Ni-MoS/unsupported catalyst exhibits a lower hydrogenation rate than the supported Ni-MoS$_2$/γ-Al$_2$O$_3$ counterpart, that is, k_2 is 1.6 times higher for Ni-MoS$_2$/γ-Al$_2$O$_3$. This difference is ascribed to the higher dispersion of the supported Ni-MoS$_2$/γ-Al$_2$O$_3$.

Evidence to assign the catalytic activity for hydrogenation to the brim sites has not been obtained. If these sites catalyze hydrogenation, a higher stacking degree should have resulted in lower hydrogenation rates because the brim sites are found only on the basal planes of the stacked layers. This would be true, however, only at a constant length of the sulfide slabs, whereas the strong variation of physical shape of the sulfide particles did not allow a detailed analysis of the impact of sites on basal planes.

The DHQ ring opening occurs by a Hofmann-type elimination to form PCHA and subsequently PCHE.[21] The Hofmann-type elimination requires an acid site for the quaternization of the N atom and a basic site for the removal of a β-H atom. This dual site consists of —SH groups with an acidic character and basic S^{2-} ions.[21,57] The trend in k_1 (ring opening of 14THQ) is correlated with the dispersion of the sulfide phase, which suggests that Ni does not play an important role in the ring opening of 14THQ. Less straightforward to understand is the trend with respect to the ring opening of DHQ (k_3), which is clearly enhanced by the presence of Ni but apparently lowered by the support. If we consider that the activity of Ni sulfides for C—N bond cleavage is lower than that of MoS$_2$,[59] it is not possible to argue that the higher value for k_3 on Ni-MoS$_2$/unsupported is because of the segregated Ni sulfide phase. Therefore, we tentatively attribute the higher value of k_3 on Ni-MoS$_2$/unsupported than on Ni-MoS$_2$/γ-Al$_2$O$_3$ to steric hindrance in the sulfide–support interface aggravated by the relatively more bulky structure of DHQ than 14THQ.

The HDS of DBT suggests that the functionality of the active sites for HDS does not depend on their position in the MoS$_2$

slabs because the selectivity does not depend on the morphology or presence of a support (Figure 16) under the conditions used in this study. The main pathway is the direct desulfurization that occurs through S σ-bonding on S vacancies (CUS). Therefore, the concentration of such CUS should correlate to the rate of the HDS reaction. For the catalysts studied, the concentration of accessible cations at the perimeter of the sulfide slabs increases as follows: Ni-MoS$_2$/unsupported $<$ MoS$_2$/γ-Al$_2$O$_3$ $<$ Ni-MoS$_2$/γ-Al$_2$O$_3$ (determined by NO adsorption). Despite the higher CUS concentration on MoS$_2$/γ-Al$_2$O$_3$, Ni-MoS$_2$/unsupported exhibits a higher HDS rate. This contrast suggests that the intrinsic rate of HDS increases because of the incorporation of Ni into the NiMoS phase. For the Ni-containing catalysts, the HDS activity is indeed determined by the dispersion of the Ni—Mo—S phase, which is higher in Ni-MoS$_2$/γ-Al$_2$O$_3$ than in Ni-MoS$_2$/unsupported.

Conclusions

A series of oxide (Ni)Mo catalyst precursors were synthesized and characterized. The supported Mo/γ-Al$_2$O$_3$ oxide material exhibited a well-dispersed amorphous polymolybdate structure. The addition of Ni causes the weaker interaction of Mo species with the support and, therefore, a higher oligomerization degree. In contrast, the unsupported NiMo material exhibited a mixture of nickel molybdate (NiMoO$_4$) and ammonium nickel molybdate ((NH$_4$)HNi$_2$(OH)$_2$(MoO$_4$)$_2$).

The sulfided, MoS$_2$/γ-Al$_2$O$_3$, Ni-MoS$_2$/γ-Al$_2$O$_3$, and Ni-MoS$_2$/unsupported active catalysts were characterized and tested in the hydrodenitrogenation (HDN) of quinoline in the presence of dibenzothiophene. The MoS$_2$ phase on the support had a high dispersion with average stacking degrees of 1.6 and 1.9 for MoS$_2$/γ-Al$_2$O$_3$ and Ni-MoS$_2$/γ-Al$_2$O$_3$, respectively, and particle lengths of 7.2 (MoS$_2$/γ-Al$_2$O$_3$) and 5.4 nm (Ni-MoS$_2$/γ-Al$_2$O$_3$). Ni-MoS$_2$/unsupported exhibited the largest stacking degree (approximately 7) and slab lengths (15–20 nm). The presence of Ni increased the concentration of coordinatively unsaturated sites (CUS) in the supported catalyst (65 μmol g^{-1} in MoS$_2$/γ-Al$_2$O$_3$ and 80 μmol g^{-1} in Ni-MoS$_2$/γ-Al$_2$O$_3$), whereas the lower CUS concentration on Ni-MoS$_2$/unsupported (33 μmol g^{-1}) was a consequence of the higher agglomeration degree.

The main route for N removal in the quinoline HDN is: quinoline→1,2,3,4-tetrahydroquinoline (14THQ; equilibrated step)→decahydroquinoline (DHQ; by hydrogenation)→propylcyclohexylamine (ring opening by C(sp^3)—N bond cleavage)→propylcyclohexene (Hofmann-type elimination by C(sp^3)—N bond cleavage)→propylcyclohexane (by hydrogenation). The ring opening of DHQ is rate determining in this sequence. The rates of N removal appreciably increase only if a significant amount of 14THQ has been converted to DHQ.

The hydrodesulfurization and hydrodenitrogenation activities follow the trend MoS$_2$/γ-Al$_2$O$_3$ $<$ Ni-MoS$_2$/unsupported $<$ Ni-MoS$_2$/γ-Al$_2$O$_3$. Ni-MoS$_2$/γ-Al$_2$O$_3$ exhibited higher rates than MoS$_2$/γ-Al$_2$O$_3$ because of the promotion by Ni. The Ni-MoS$_2$/unsupported catalyst exhibited lower rates than Ni-MoS$_2$/γ-Al$_2$O$_3$, likely because of the low dispersion of the former. Ni-MoS$_2$/unsupported is more active than MoS$_2$/γ-Al$_2$O$_3$ despite the higher

CUS concentration in the latter. Therefore, Ni-MoS$_2$/unsupported exhibited higher intrinsic rates because of the promotion mechanisms of Ni species. In turn, although we attribute the promoter effect to the formation of the Ni—Mo—S phase (Ni atoms that decorate MoS$_2$) on the support, we propose that in the unsupported catalyst, particles of Ni$_x$S$_y$ also form at the MoS$_2$ edges that exert a promoter effect (albeit weaker than the single Ni atom decoration effect). The ring-opening steps are the only ones that seem to be more influenced by the morphology of the sulfide phase than by the presence of promoter.

Experimental Section

Catalyst preparation

The oxide precursors of the supported Mo and NiMo catalysts were prepared by the two-step incipient wetness impregnation of γ-Al$_2$O$_3$ (237 m^2 g^{-1}). Prior to impregnation, the support was dried at 120 °C in static air and treated at 560 °C for 2 h under synthetic air flow. In the first step, the carrier was impregnated with an aqueous solution of ammonium heptamolybdate, (NH$_4$)$_6$Mo$_7$O$_{24}$·4H$_2$O (99.98 %, Aldrich). After impregnation, the catalyst was dried at 120 °C overnight in static air atmosphere and then treated at 500 °C for 4 h (heating rate of 1 °C min^{-1}) under synthetic air flow. Part of the prepared sample was preserved as the oxidic Mo catalyst precursor and the other was used as a support for the impregnation with an aqueous solution of nickel nitrate, Ni(NO$_3$)$_2$·6H$_2$O ($\geq$ 98.5 %, Aldrich). After impregnation, the NiMo precursor was thermally treated as in the case of the Mo precursor. The Mo concentration in the Mo and NiMo oxide precursors was 8.6 wt % (2.5 atom nm^{-2}), whereas the Ni concentration in the NiMo precursor was 3.6 wt %.

The sulfide catalysts were obtained by sulfidation of the oxide precursors under 10 % H$_2$S in H$_2$ flow at 400 °C and 1.8 MPa for 8 h. After cooling to RT in the sulfiding agent, the catalysts were flushed with H$_2$ and stored under a N$_2$ atmosphere. Hereafter, the oxidic precursors are referred to as Mo/γ-Al$_2$O$_3$ and NiMo/γ-Al$_2$O$_3$, whereas the corresponding supported sulfide catalysts are denoted as MoS$_2$/γ-Al$_2$O$_3$ and Ni-MoS$_2$/γ-Al$_2$O$_3$.

The oxide precursor of the unsupported catalyst was prepared by coprecipitation.[60] Ammonium heptamolybdate, (NH$_4$)$_6$Mo$_7$O$_{24}$·4H$_2$O (Aldrich), was dissolved in doubly distilled water at RT in a three-necked flask equipped with a reflux condenser. Aqueous ammonia (28–30 %) was added under continuous stirring until the pH of the solution changed from 5.5 to 9.5. In parallel, an aqueous solution of nickel nitrate, Ni(NO$_3$)$_2$·6H$_2$O (Aldrich; pH 6), was heated to 60 °C and then added dropwise to the ammonium heptamolybdate solution (kept at 90 °C). A light green precipitate formed at pH 7 was collected by filtration. The filter cake was dispersed into maleic acid solution (0.05 mol l^{-1}, pH 1.5) to form a slurry (pH 6). After filtration, the collected precipitate was vacuum dried overnight at RT and further dried at 120 °C for 12 h (heating rate of 1 °C min^{-1}) under a flow of synthetic air. The sulfidation of the unsupported catalyst precursor was performed under a 10 % H$_2$S in H$_2$ flow at 400 °C and 1.8 MPa for 12 h. After cooling to RT in the sulfiding agent, the catalyst was flushed with H$_2$ and stored under a N$_2$ atmosphere. The oxidic precursor is denoted as NiMo/unsupported, and the sulfide catalysts as Ni-MoS$_2$/unsupported.

Catalyst characterization

The BET surface areas and pore size distributions were determined from the analysis of the N_2 adsorption–desorption isotherms of the oxidic precursors at $-196\,°C$. A PMI Automated BET Sorptomatic 1900 Series instrument (Thermo Finnigan) was used to perform the experiments. Prior to the adsorption, the supported samples were evacuated at $250\,°C$ for 2 h, and the unsupported catalyst precursor was evacuated at $120\,°C$ for 4 h. Elemental analysis was performed at the Microanalytical Laboratory of the TU München.

NO adsorption was performed as a pulse experiment at RT to probe the concentration of adsorption sites and average edge dispersion in the studied metal sulfide catalysts. A detailed description of the experiment can be found elsewhere.[15]

The crystal structure of the samples was determined by analysis of the powder XRD patterns. The crystallographic phases were identified by using the inorganic crystal structure database (ICSD).[20] The XRD patterns were collected by using a Philips X'Pert System (CuK$_\alpha$ radiation, 0.1542 nm) using a NiK$_\beta$ filter and a solid-state detector (X'Celerator). The operating conditions were 45 kV and 40 mA. The prepared catalysts were measured with a step size of $0.017°$ and a scan time of 115 s per step. Selected reference materials were measured over 5 min with a step size of $0.017°$ and a scan time of 10 s per step.

The Scherrer equation was used to determine the stacking degree of the sulfide slabs in the unsupported catalyst in the knowledge that the diffraction at $2\theta = 14°$ corresponds to the (0 0 2) plane with an interplanar distance of 6.1 Å (distance between the Mo layers in MoS_2) [Eq. (1)]:

$$L = \frac{K \cdot \lambda}{\Delta(2\theta) \cdot \cos\theta} \tag{1}$$

in which L is the mean size of ordered (crystalline) domain, K is the Scherrer shape factor (0.9), λ is the X-ray wavelength used, θ is the measured Bragg angle, and $\Delta(2\theta)$ is the line broadening [rad]. To calculate the line broadening Equation (2) was used:

$$\Delta(2\theta) = \text{FWHM} - 0.1 \tag{2}$$

in which FWHM is the full width at the half maximum [rad], and 0.1 is the typical instrument parameter.

Electron microscopy measurements were performed in the transmission mode coupled with selective area electron diffraction (TEM-SAD) and in scanning mode at high resolution coupled with energy-dispersive X-ray spectroscopy (HR-SEM-EDX). Samples of the catalysts were ground and ultrasonically dispersed in ethanol. Drops of the dispersion were applied to a copper-carbon grid. TEM and SAD measurements were performed by using a JEOL JEM-2011 TEM instrument with an accelerating voltage of 120 keV. For the HR-SEM and EDX mapping measurements, a high-resolution field emission (FE) SEM JSM 7500 F (JEOL) instrument with EDX (Oxford) was used. The micrographs were recorded with a secondary electron imaging (SEI) detector and an accelerating voltage of 5 keV.

Raman spectra were obtained with a 514 nm Ar laser by using a Renishaw Raman Spectrometer (Type 1000) equipped with a charge-coupled device (CCD) detector and a Leica microscope DM LM. Prior to the measurements, calibration was performed with a Si(111) crystal. The wavenumber accuracy was within $1\,cm^{-1}$. The oxidic catalyst precursors and reference materials were analyzed

under ambient conditions in the form of self-supported wafers. In situ measurements were performed by placing the sample into a quartz capillary connected to a flow system and attached to a heating wire. The sulfidation was performed under $10\%\ H_2S$ in H_2 at $400\,°C$ for 1 h, and spectra were recorded every $100\,°C$. Afterwards the sample was cooled to RT, and the flow was switched to N_2 to record further spectra. Finally, the sample was heated to $400\,°C$ again under a flow of synthetic air to acquire the final spectra.

The diffuse reflectance technique was applied to collect UV/Vis/near IR spectra by using an Avantes AvaSpec-2048 fiber optic spectrometer equipped with a CCD detector array. A combined deuterium and halogen light source, Ava Light-DH-S-BAL, was used in combination with a fiber optic cable FCR-7V400-2-SR-HT. Spectra of oxide catalyst precursors and reference materials were recorded under ambient conditions. The samples were placed as powders in a Teflon sample holder that provided 1 mm sample thickness.

The structural properties of the oxide catalyst precursors, the sulfided catalysts, and the materials during the catalyst sulfidation were studied in situ by X-ray absorption spectroscopy (XAS) at the X1 beamline at Hasylab, DESY, Hamburg, Germany. The data set was completed with experiments performed on the BM 26A—DUBBLE, (Dutch-Belgian) beamline at the ESRF, Grenoble, France. Spectra were recorded in the transmission mode at the Mo K-edge (20 000 eV) using Si (3 1 1) crystals and at the Ni K-edge (8333 eV) using Si (1 1 1) crystals in the monochromator, respectively. The contributions of the higher harmonics were minimized by detuning the second crystal of the monochromator to 60% of the maximum intensity. Energy calibration was performed with Mo and Ni metal foils, respectively, measured simultaneously with the samples. The samples were prepared as self-supported wafers placed in a stainless-steel in situ flow cell. The measured reference compounds were mixed with cellulose to achieve a total absorption of $\mu x = 1.5$. The spectra of the oxide precursors, sulfided catalysts, and reference compounds used for EXAFS analysis were collected in He flow and at liquid N_2 temperature (LNT) to minimize thermal vibrations. At least two spectra of each sample were averaged to enhance the signal-to-noise ratio. After the EXAFS measurements of the oxidic catalyst precursors, quick XAFS scans with a resolution of 180 s were recorded continuously during the catalyst sulfidation under a flow of $10\%\ H_2S$ in H_2 with a heating rate of $5\,°C\,min^{-1}$ up to $400\,°C$ followed by an isothermal period of 1 h.

Quick XAFS data were processed by using XANES dactyloscope software (version 2012/4).[61] The scattering contributions in the pre- and postedge of the background were removed from the X-ray absorption by using a third-order polynomial function, and all spectra were normalized to the average postedge height of one. The XANES and EXAFS data were analyzed by using IFEFFIT using the Horae package (ATHENA and ARTEMIS, version 1.2.11).[62,63] After the removal of the background absorption and normalization, the oscillations were weighted with k^3 and Fourier transformed within the limit of 3.5–14 $Å^{-1}$ for the oxide precursor and $k = 3–12.0\ Å^{-1}$ for the sulfided catalyst. The local environments of the Mo and Ni atoms in the sulfided catalysts were determined in k space from the EXAFS data. Single and multiple scattering contributions for Mo–S, Mo–Mo, Ni–S, and Ni–Ni (phase shifts and backscattering amplitudes) were calculated with FEFF[64] by using the geometries of the crystallographic information files (cif) of the ICSD.[20] The amplitude reduction factor S_0^2 was determined from reference compounds and found to be 1.16 for Mo and 1.00 for Ni. For Ni-MoS$_2$/γ-Al$_2$O$_3$ and Ni-MoS$_2$/unsupported, the EXAFS data at the Mo K-edge and at the Ni K-edge were simultaneously fitted

to identify Mo–Ni and Ni–Mo contributions, respectively. The Debye–Waller factor σ^2 and the distance R between Mo–Ni and Ni–Mo were constrained to be equal, and the coordination numbers N for Mo–Ni and Ni–Mo were constrained by the molar ratio of Ni and Mo in the catalysts ($N_{Mo–Ni} = n(Ni)/n(Mo) \cdot N_{Ni–Mo}$).

TPS was performed to study the influence of Ni on the sulfidation mechanism. The oxide precursor (0.1 g) was placed in a flow reactor equipped with a ceramic oven. The activation was performed under 10% H_2S in H_2 with a heating rate of 5 °C min^{-1}. At 400 °C, the temperature was held isothermally for 1 h. The evolved gasses were detected by a quadrupole mass spectrometer (Balzers QME 200).

Catalytic performance

The HDN of quinoline (Q) was studied in the presence of DBT in a continuous-flow trickle-bed reactor system at constant feed composition and a pressure of 5.0 MPa. The reactor was loaded with oxide catalyst precursor (0.05 g) for each run. Gas and liquid feeds were introduced into the reactor by high-pressure mass flow meters (Bronkhorst) and an HPLC pump (Shimadzu LC-20AD), respectively. After the separation of the liquid and gas effluent phase, the liquid was collected by a 16-port sampling valve every 1.5 h. The liquid samples were analyzed by off-line GC by using a HP 6890 GC equipped with a flame ionization detector (FID) and 60 m DB-17 capillary column.

Prior to the kinetic experiments, the catalysts were activated in situ under a 10% H_2S in H_2 flow at 400 °C and 1.8 MPa for 12 h. HDN was investigated in space-time-dependent experiments at 370 °C. The space time was defined as $m_{cat}F_N^{-1}$, in which m_{cat} is the amount of the oxide catalyst precursor and F_N is the molar flow of Q [h g$_{catalyst}$ mol$_Q^{-1}$]. Additionally, HDN was performed as temperature-dependent experiments (290–400 °C) at a constant space time of 350 h g$_{cat}$ mol^{-1}. Steady state was reached after 16 h time on stream. All reactions were performed under an excess of H_2 with a constant H_2-to-hydrocarbon ratio of 330 Ndm^3 dm^{-3}. The initial concentration of Q (Aldrich, 98%) was set to 1000 ppm wt N (equivalent to 14.6 kPa of Q) in a mixture of 5% hexadecane (Merck, 99%) in tetradecane (Alfa Aesar, 99+%) as a solvent. DBT (Aldrich, 99%) was added at a concentration of 500 ppm wt S (equivalent to 3.2 kPa of DBT). The conversion towards N-free products is referred to the HDN conversion. For a more detailed description, see Ref. [21].

Acknowledgements

[1] F. Besenbacher, M. Brorson, B. S. Clausen, S. Helveg, B. Hinnemann, J. Kibsgaard, J. V. Lauritsen, P. G. Moses, J. K. Nørskov, H. Topsøe, *Catal. Today* **2008**, *130*, 86–96.

[2] R. Prins, V. H. J. de Beer, G. A. Somorjai, *Catal. Rev. Sci. Eng.* **1989**, *31*, 1–41.

[3] H. Topsøe, *Appl. Catal. A* **2007**, *322*, 3–8.

[4] M. Daage, R. R. Chianelli, *J. Catal.* **1994**, *149*, 414–427.

[5] O. Gutiérrez, T. Klimova, *J. Catal.* **2011**, *281*, 50–62.

[6] G. Berhault, M. De La Rosa, A. Mehta, M. Yácaman, R. Chianelli, *Appl. Catal. A* **2008**, *345*, 80–88.

[7] S. Eijsbouts, L. van den Oetelaar, R. van Puijenbroek, *J. Catal.* **2005**, *229*, 352–364.

[8] G. Perot, *Catal. Today* **1991**, *10*, 447–472.

[9] J. van Gestel, J. Leglie, J. C. Duchet, *Appl. Catal. A* **1992**, *92*, 143–154.

[10] M. Jian, R. Prins, *Catal. Today* **1996**, *30*, 127–134.

[11] L. Qu, R. Prins, *Appl. Catal. A* **2003**, *250*, 105–115.

[12] N. Y. Topsøe, A. Tuxen, B. Hinnemann, J. V. Lauritsen, K. G. Knudsen, F. Besenbacher, H. Topsøe, *J. Catal.* **2011**, *279*, 337–351.

[13] F. Mauge, J. Lamotte, N. S. Nesterenko, O. Manoilova, A. A. Tsyganenko, *Catal. Today* **2001**, *70*, 271–284.

[14] R. W. G. Wyckoff in *Crystal Structures, Vol. 1*, Interscience, New York, **1963**, pp. 280–281.

[15] A. Hrabar, J. Hein, O. Y. Gutiérrez, J. A. Lercher, *J. Catal.* **2011**, *281*, 325–338.

[16] F. Pedraza, J. Cruz-Reyes, D. Acosta, M. J. Yañez, M. Avalos-Borja, S. Fuentes, *J. Phys. Condens. Matter* **1993**, *5*, A219.

[17] J. L. Verble, T. J. Wieting, *Phys. Rev. Lett.* **1970**, *25*, 362–365.

[18] T. J. Wieting, J. L. Verble, *Phys. Rev. B* **1971**, *3*, 4286–4292.

[19] S. M. A. M. Bouwens, R. Prins, V. H. J. de Beer, D. C. Koningsberger, *J. Phys. Chem. A* **1990**, *94*, 3711–3718.

[20] A. Belsky, M. Hellenbrandt, V. L. Karen, P. Luksch, *Acta Crystallogr. Sect. B* **2002**, *58*, 364–369.

[21] O. Y. Gutiérrez, A. Hrabar, J. Hein, Y. Yu, J. Han, J. A. Lercher, *J. Catal.* **2012**, *295*, 155–168.

[22] T. C. Ho, *Appl. Catal. A* **2010**, *378*, 52–58.

[23] P. Afanasiev, *J. Catal.* **2010**, *269*, 269–280.

[24] C. N. Satterfield, J. F. Cocchetto, *Ind. Eng. Chem. Process Des. Dev.* **1981**, *20*, 53–62.

[25] J. F. Cocchetto, C. N. Satterfield, *Ind. Eng. Chem. Process Des. Dev.* **1976**, *15*, 272–277.

[26] I. E. Wachs, *Catal. Today* **1996**, *27*, 437–455.

[27] C. P. Cheng, G. L. Schrader, *J. Catal.* **1979**, *60*, 276–294.

[28] H. Hu, I. E. Wachs, S. R. Bare, *J. Phys. Chem.* **1995**, *99*, 10897–10910.

[29] N. F. D. Verbruggen, G. Mestl, L. M. J. von Hippel, B. Lengeler, H. Knözinger, *Langmuir* **1994**, *10*, 3063–3072.

[30] H. Jeziorowski, H. Knözinger, *J. Phys. Chem.* **1978**, *82*, 2002–2005.

[31] H. Jeziorowski, H. Knözinger, *J. Phys. Chem.* **1979**, *83*, 1166–1173.

[32] H. Aritani, T. Tanaka, T. Funabiki, S. Yoshida, M. Kudo, S. Hasegawa, *J. Phys. Chem.* **1996**, *100*, 5440–5446.

[33] B. Canosa-Rodriguo, H. Jeziorowski, H. Knözinger, X. Wang, E. Taglauer, *Bull. Soc. Chim. Belg.* **1981**, *90*, 1271–1278.

[34] E. Payen, J. Grimblot, S. Kasztelan, *J. Phys. Chem.* **1987**, *91*, 6642–6648.

[35] D. Levin, S. Soled, J. Ying, *Inorg. Chem.* **1996**, *35*, 4191–4197.

[36] R. Cattaneo, T. Weber, T. Shido, R. Prins, *J. Catal.* **2000**, *191*, 225–236.

[37] H. Topsøe, B. S. Clausen, F. E. Massoth in *Hydrotreating Catalysis Science and Technology*, Springer, Berlin & Heidelberg, **1996**.

[38] J. V. Lauritsen, M. Nyberg, J. K. Nørskov, B. S. Clausen, H. Topsøe, E. Laegsgaard, F. Besenbacher, *J. Catal.* **2004**, *224*, 94–106.

[39] B. S. Clausen, H. Topsøe, R. Candia, J. Villadsen, B. Lengeler, J. Als-Nielsen, F. Christensen, *J. Phys. Chem.* **1981**, *85*, 3868–3872.

[40] T. G. Parham, R. P. Merrill, *J. Catal.* **1984**, *85*, 295–310.

[41] L. S. Byskov, J. K. Nørskov, B. S. Clausen, H. Topsøe, *J. Catal.* **1999**, *187*, 109–122.

[42] J. V. Lauritsen, S. Helveg, E. Lægsgaard, I. Stensgaard, B. S. Clausen, H. Topsøe, F. Besenbacher, *J. Catal.* **2001**, *197*, 1–5.

[43] F. L. Deepak, R. Esparza, B. Borges, X. Lopez-Lozano, M. J. Yacaman, *ACS Catal.* **2011**, *1*, 537–543.

[44] N. Koizumi, Y. Hamabe, S. Jung, Y. Suzuki, S. Yoshida, M. Yamada, *J. Synchrotron Radiat.* **2010**, *17*, 414–424.

[45] S. P. A. Louwers, R. Prins, *J. Catal.* **1992**, *133*, 94–111.

[46] H. Topsøe, B. Clausen, *Appl. Catal.* **1986**, *25*, 273–293.

[47] C. Wivel, B. S. Clausen, R. Candia, S. Mørup, H. Topsøe, *J. Catal.* **1984**, *87*, 497–513.

[48] R. Candia, B. S. Clausen, H. Topsøe, *J. Catal.* **1982**, *77*, 564–566.

[49] B. Yoosuk, J. H. Kim, C. Song, C. Ngamcharussrivichai, P. Prasassarakich, *Catal. Today* **2008**, *130*, 14–23.

[50] M. Ramos, G. Berhault, D. A. Ferrer, B. Torres, R. R. Chianelli, *Catal. Sci. Technol.* **2012**, *2*, 164–178.

[51] R. R. Chianelli, *Oil Gas Sci. Technol.* **2006**, *61*, 503–513.

[52] Y. Okamoto, H. Okamoto, T. Kubota, H. Kobayashi, O. Terasaki, *J. Phys. Chem. B* **1999**, *103*, 7160–7166.

[53] S. Eijsbouts, *Appl. Catal. A* **1997**, *158*, 53–92.

[54] A. N. Startsev, *Catal. Rev. Sci. Eng.* **1995**, *37*, 353–423.

[55] M. Breysse, E. Furimsky, S. Kasztelan, M. Lacroix, G. Perot, *Catal. Rev. Sci. Eng.* **2002**, *44*, 651–735.

[56] P. Clark, W. Wang, P. Deck, S. T. Oyama, *J. Catal.* **2002**, *210*, 116–126.

[57] L. S. Byskov, J. K. Nørskov, B. S. Clausen, H. Topsøe in *Transition Metal Sulphides—Chemistry and Catalysis* (Eds.: T. Weber, R. Prins, R. A. van Santen), Kluwer, Dordrecht, **1998**.

[58] F. E. Massoth, G. Muralidhar, J. Shabtai, *J. Catal.* **1984**, *85*, 53–62.

[59] J. Shabtai, Q. Guohe, K. Balusami, N. K. Nag, F. E. Massoth, *J. Catal.* **1988**, *113*, 206–219.

[60] T. Maesen, A. E. Kuperman, US 2009/0107883 A1.

[61] K. V. Klementiev, *XANES Dactyloscope* for Windows Version **2012/4**, freeware: www.cells.es/Beamlines/CLAESS/software/xanda.html.

[62] M. Newville, *J. Synchrotron Radiat.* **2001**, *8*, 322–324.

[63] B. Ravel, M. Newville, *J. Synchrotron Radiat.* **2005**, *12*, 537–541.

[64] A. L. Ankudinov, J. J. Rehr, *Phys. Rev. B* **2000**, *62*, 2437–2445.